

A NOVEL APPROACH TO ATMOSPHERIC PROFILING WITH A DOWN-LOOKING MOUNTAIN-BASED OR AIR-BORNE GPS RECEIVER

Cinzia Zuffada, George A. Hajj, E. Robert. Kursinski

Jet Propulsion Laboratory
California Institute of Technology
Pasadena, CA 91109

ABSTRACT

The delay induced by the Earth's atmosphere on the Global Positioning System (GPS) signal has been exploited in the last decade for atmospheric remote sensing. Ground-based GPS measurements are traditionally used to derive columnar water vapor content while space-based GPS measurements obtained by tracking GPS satellites occulting behind the Earth's atmosphere, as viewed by a receiver in a low-Earth orbit, have been demonstrated to yield very accurate high resolution profiles of refractivity, temperature and water vapor. A GPS receiver on a balloon, airplane or mountain top with a "downward-looking" field of view toward the Earth's limb is a novel concept which is presented here. This new remote sensing approach provides dense coverage of high vertical resolution profiles of refractivity in the region around the receiver, which yield much needed information on boundary layer structure and complement the columnar moisture data from upward looking receivers for regional hydrological research. We present a generalized raytracing inversion scheme which can be used when occultation data is acquired with a receiver within (e.g., on mountain top) or outside (i.e., in space) the atmosphere. In this scheme, spherical symmetry is assumed for the atmosphere and the refractivity is modeled as piecewise

exponential, with scale height changing from one atmospheric layer to the next. Additional refractivity data derived from a model might be introduced at high altitude, and are treated as properly weighted measurements. The exponential scale heights and a normalizing value of refractivity are retrieved by minimizing the residuals between measured bending angles and refractivity and those calculated based on the exponential model. We first illustrate results comparing refractivity and temperature profiles obtained by this generalized raytracing scheme against those derived via the Abel inversion for the GPS/MET experiment. Additionally, we present results for a hypothetical situation where the receiver is located on an ascending balloon reaching the maximum height of 25 km, and finally for a receiver placed within the atmosphere at a height of 5 km. For the last case we investigate the accuracy of the retrieval both below and above the receiver at a set of locations in the atmosphere ranging from mid to tropical latitudes. Our findings suggest that the GPS data collected from inside the atmosphere has enough strength to allow for quite accurate retrievals of refractivity at heights up to several km above the receiver locations.

1. INTRODUCTION

Radio occultation measurements using the Global Positioning System (GPS) and a receiver in low-Earth orbit (LEO) have recently been shown to provide accurate profiles of atmospheric refractivity, pressure, water vapor and temperature with high vertical resolution [e.g. Hajj et al., 1995; Kursinski et al., 1996; Ware et al., 1996; Leroy, 1997; Rocken et al., 1997; Kursinski and Hajj, 1998]. The high accuracy and resolution of atmospheric profiles obtained from GPS occultations at a relatively low cost, has created considerable interest in the atmospheric and climate research communities, because of the data's potential impact. For instance, several studies have investigated means of

assimilating GPS occultation data into numerical weather predictions and the impact this data would have on the models [Eyre, 1994; Zou *et al.*, 1995; Kuo *et al.*, 1998; Zou *et al.*, 1998], while others examined the climate information content of this data [Yuan *et al.*, 1993; Kursinski and Hajj, 1998; Leroy, 1998].

While GPS occultation data collected from space has the advantage of being global (one receiver in low-Earth orbit provides about 500 globally distributed occultations per day), the sampling in any particular region is relatively sparse without a large number of orbiting receivers. (For a review of the space-based GPS occultation technique see, e.g., Kursinski *et al.*, 1997.) By contrast, a receiver located inside the Earth's atmosphere (such as on a mountain top, a balloon, or an airplane) can be used to provide data over specific areas of interest for the purpose of regional weather and climate studies, and atmospheric and coupled ocean/atmospheric process research. A mountain-based or air-borne receiver would track any GPS satellite as it sets or rises behind the Earth's limb, therefore collecting data at both negative and positive elevations relative to the receiver's local horizon (Figure 1). We have found that by combining both the negative and positive elevation data we obtain a high resolution profile of refractivity below the receiver's height, and a coarser resolution profile extending a few kilometers above the receiver.

The viewing geometry of a "down-looking" GPS receiver located inside the atmosphere can be thought of as a hybrid between the space and ground viewing geometries; it combines the high vertical profiling capability of space data (limited to the heights below the receiver) with the benefit of routinely obtaining 10's of daily profiles in regions of interest. One receiver with a full 360 degrees field of view of the horizon will observe as many as 96 occultations per day scattered around the receiver. Each occultation will yield a profile of refractivity below the receiver's height with a vertical resolution of 150-250 meters. Refractivity in turn can be converted to a profile of water vapor with an accuracy

of about 0.2 g/kg by assuming knowledge of temperature from a numerical weather model (as done by *Kursinski and Hajj*, 1998). This observing geometry, therefore, provides a very accurate and efficient means of sensing water vapor and the boundary layer structure in specific regions of interest.

The goal of this paper is to introduce this concept for the first time, illustrate a raytracing inversion scheme suitable for this special sensing geometry, and examine the achievable accuracy, resolution, and the usefulness of this technique.

The raytracing-based inversion technique developed here can be considered a generalization of the more traditional “Abel transform” inversion normally used in space-based atmospheric occultation. The challenge associated with inverting data from a down-looking air-borne receiver is that data collected at positive elevations is only weakly sensitive to the atmospheric vertical structure above it, while obtaining an accurate retrieval below the receiver requires a somewhat accurate knowledge of the refractivity profile above the receiver. A solution to this problem, which is pursued here, is to combine both negative and small-angle positive elevation data in an optimal manner.

The technique presented below can also be used in assimilating GPS occultation data (space-based or air-borne) in numerical weather prediction (NWP). In this context, this technique would be relevant to other research on assimilating space-based GPS occultation data into numerical weather models [*Eyre*, 1994; *Gorbunov*, 1996; *Kuo et al.*, 1996; *Zou et al.*, 1998]. Specifically, if retrieved profiles of refractivity were to be assimilated in NWP according to the schemes outlined in the referenced work, the technique described in this paper could be used in the phase of inversion of the bending measurements. It is noted that the specific inversion implemented in our work is more accurate than the scheme outlined by *Eyre* [1994] for representing the behavior of refractivity in each atmospheric layer when

spherical symmetry applies. On the other hand, the scheme suggested by *Eyre* [1994] to account for the horizontal gradients of refractivity could be incorporated into our work in the future.

This paper is structured as follows: In section 2 we give a brief summary of the GPS occultation technique and the traditional Abel inversion scheme (sec. 2.1) and then a detailed description of the new scheme suitable for air-borne occultation measurements (sec. 2.2), hereafter referred to as JPL (raytracing) inversion scheme. In section 3 we compare the raytracing inversion scheme to the Abel inversion, by applying it on data collected from space with the GPS/MET experiment¹. In section 4 we use the new technique in two simulated applications: first, the receiver is assumed to be on a balloon at 25 km height, second, the receiver is assumed to be fixed at 5 km altitude. Several examples are considered from which conclusions are drawn. Section 5 presents a summary and conclusions.

2. INVERSION SCHEMES

In a spherically symmetric medium, a signal travels along a curve defined by

$$nr \sin(\phi) = \text{constant} \equiv a \quad (1)$$

where r is the distance from the origin of symmetry to a point on the raypath, ϕ is the angle between the direction of r and the tangent to the raypath, n is the index of refraction at r . Eq. (1) corresponds to Snell's law in polar coordinates for a spherically symmetric

¹ GPS/MET is a proof-of-concept experiment which carried a GPS receiver into space for the purpose of atmospheric occultation. It started in 1995 and collected over 2 years worth of occultation data. It is managed by the University Corporation for Atmospheric Research, Boulder, Colorado.

medium, and it is also known as Bouguer's formula. Based on this a signal traveling in a spherically symmetric medium will bend by an amount [*Born and Wolf*, 1980]

$$\alpha = a \int_{raypath} \frac{1}{n\sqrt{n^2 r^2 - a^2}} \frac{dn}{dr} dr \quad (2)$$

When the receiver is outside the atmosphere, a corresponds to the asymptote miss distance or impact parameter.

The basic observables of the GPS satellites from which the bending is derived are the L1 (wavelength = 19.0 cm) and L2 (wavelength = 24.4 cm) phase delays. From knowledge of the positions of the transmitter and the receiver and their clocks (which are obtained from other GPS measurements collected simultaneously), the delay due to the intervening media can be isolated. Both L1 and L2 signals are used to calibrate for the dispersive ionosphere, and the extra neutral atmospheric delay is isolated. (For a more detailed discussion of how atmospheric delay is detected see e.g., *Hajj et al.*, 1995.) From knowledge of the atmospheric extra delay as a function of time, we can derive the extra atmospheric Doppler which can be related to the bending of the signal via the equation

$$\Delta f = \frac{f}{c} \left(\vec{v}_t \cdot \vec{k}_t - \vec{v}_r \cdot \vec{k}_r - \{\vec{v}_t - \vec{v}_r\} \cdot \vec{k} \right) \quad (3)$$

where f is the GPS transmitting frequency, c is the speed of light, \vec{v}_t and \vec{v}_r are the transmitter and receiver velocities, respectively, \vec{k}_t and \vec{k}_r are the unit vectors in the direction of the transmitted and received signal, respectively, and \vec{k} is the unit vector in the direction of the straight line passing through the transmitter and receiver positions (Figure 2).

From Eq. (2) and the following equation which is implied by Bouguer's formula:

$$a = r_t n_t \sin(\theta_t + \delta_t) = r_r n_r \sin(\theta_r + \delta_r) \quad (4)$$

(angles are defined in Figure 2) we can derive the total bending of the signal ($\alpha = \delta_t + \delta_r$) as a function of a . Note that Eqs. (1)-(4) can be applied to GPS data received at either positive or negative elevation. The fundamental function to be inverted is $\alpha(a)$. Figure 3 shows $\alpha(a)$ for both space-based and air-borne occultation geometries. The particular features of this function for the two different geometries (receiver inside and outside the atmosphere) are discussed below.

2.1 Abel Inversion Scheme

The Abel inversion has been used extensively in seismic inversions as well as in inverting planetary and Earth occultation data [see e.g., *Fjeldbo et al.*, 1971 or *Kursinski et al.*, 1997]; therefore, we describe it here very briefly and point out its limitations. Once the bending is determined, then Eq. (2) can be inverted with an Abelian transformation [e.g., *Tricomi*, 1977] to solve for n as

$$\ln(n(a)) = \frac{1}{\pi} \int_a^\infty \frac{\alpha(a')}{\sqrt{a'^2 - a^2}} da' \quad (5)$$

Note that the upper limit of the integral is infinity, which makes it necessary to have measurements of α starting from outside the atmosphere (where α vanishes) for this integral to be performed. When the receiver lies inside the atmosphere at radius r_r , then only measurements of $\alpha(a)$ for $a < r_r$ are available; therefore, Eq. (5) cannot be used.

2.2 Raytracing -based Inversion Technique

In essence our raytracing technique models the atmosphere as a set of concentric layers of specified thickness, with refractivity varying exponentially as a function of radius with a fixed scale height for each layer. The inversion consists of finding the optimal set of scale heights and an overall normalization factor that best fit the measured bending angles and other given information or measurements. Since each bending measurement at negative elevation is heavily weighted by the atmospheric structure at the layer where the tangent point resides, the atmospheric structure below the receiver's height can, to some extent, be uniquely determined from these negative elevation measurements. In addition, we will demonstrate that refractivity at the receiver's height and immediately above it (by 1-2 km) can be uniquely retrieved without the help of other information. As we start going to higher elevation, data becomes strongly correlated, and we must rely on other *a priori* information or measurements to be able to obtain a unique solution for the atmosphere at higher altitudes.

2.2.1 Data Smoothing and Layering

When the receiver is outside the atmosphere, bending measurements are smoothed over the time it takes the tangent height of the ray to descend the diameter of the first Fresnel zone [Kursinski *et al.*, 1997]. In the geometrical optics framework these smoothed

measurements are approximately independent. Layer boundaries are then placed between the tangent point of each of the measurements. (Even though α_i is given as a function of a_i , the radius of the tangent point corresponding to that measurement, and therefore its height, is estimated by solving the relation $a = r n(r)$ where $n(r)$, the index of refraction at r , is obtained from an *a priori* model introduced as a first guess at the solution).

When a receiver is inside the atmosphere, we group the bending measurements α_i into a set of m_a ‘negative elevation’ measurements and a set of m_p ‘positive elevation’ measurements (Figure 1). Distinguishing between positive and negative elevation is possible based on the variation of Eq. (1) and the impact on bending. The typical behavior of the bending $\alpha(a)$ is illustrated in the large scale features of Figure 3.b where, for a fixed receiver, the transition between negative and positive elevation data corresponds to the maximum a of the α vs. a curve. This follows from Eq. (1) which implies that, coming from positive elevation measurements, a is maximum when the signal is received at zero elevation (since $nr - r$ is the radius of the receiver in this case— is constant). On the other hand, moving toward negative elevation, a is also maximum when the signal is received at zero elevation since r —which is now the radius of the tangent point— is decreasing as the signal descends to lower elevations (the increase in n is usually not large enough to change the derivative of nr). When the receiver is moving inside the atmosphere, separating positive and negative elevation data can be more difficult, depending on the dynamics of the motion. However, in most practical situations, such as a receiver on a balloon or an airplane, the motion will be slow enough such that a similar, although more complicated, treatment is possible.

Smoothing of negative elevation data and layering below the receiver are treated in exactly the same way as space-based measurements in the manner described above. However, for positive elevation data, there is no well defined smoothing time for which data can be considered independent. In fact, positive elevation data become strongly correlated soon after the elevation is a few degrees above zero. In general, it is expected that, due to their diminishing strength, those measurements corresponding to the first few degrees above the horizon will play the most important role in retrieving the refractivity at and above the receiver. The time smoothing is then determined such that data points are obtained at specified elevations. Layers' thickness immediately above the receiver (by 1-2 km) are chosen to be commensurate to those below the receiver; we denote the number of these layers by m_u . As we move higher, the thickness of the layers are chosen to be commensurate to the resolution of some *a priori* atmospheric model, or to the resolution of other types of measurements (e.g., radiosonde) if available; we denote the number of these layers by m_n .

As explained above, the $\alpha_i(a_i)$ are complemented by a set of values for refractivity above the receiver (N_i , $i=1, m_n$). These values are obtained from an *a priori* model or other measurements. It is noted that each measurement has an associated error, which is used to weigh the correspondent equation in the solution process. Throughout this work the refractivity N obtained from the *a priori* model is weighted by assuming it to have a Gaussian distribution with $\sigma = 0.05N$. By contrast, for the bending measurements we have estimated $\sigma = 0.01\alpha + 10^{-5}$ (radians). This value comprises the error due to the spherical symmetry approximation (first addendum, dominant at low altitudes) and to the receiver thermal noise (second addendum, dominant at high altitudes).

We assume refractivity to be changing exponentially with a constant scale height within each layer. In what follows we will refer to this layering of the atmosphere as the “exponential model” (to distinguish it from the *a priori* model). This exponential model, therefore, consists of $m_L = m_a + m_u + m_n$ layers, with m_L scale heights. Given these scale heights, and constraining the refractivity (but not its derivative) to be continuous across the boundaries of different layers, we can write a functional form that describes refractivity everywhere in the atmosphere as a function of r , the radial distance from the earth’s center to a point in layer j , where $R_{j+1} > r > R_j$, as

$$N(r) = N_{norm} \exp\left(-\frac{r - R_j}{H_j}\right) \prod_{i=j+1}^{m_L} \exp\left(-\frac{\Delta_i}{H_i}\right) \quad (6)$$

where R_j is the lower boundary of the j^{th} layer, Δ_i and H_i are the i^{th} layer thickness and scale height, respectively. In Eq. (6) we introduce one additional parameter, the normalization factor of refractivity, N_{norm} . Initial values of N_{norm} and H_i ‘s are obtained from the *a priori* model.

2.2.2 Inversion Scheme

Eq. (6) represents our model for atmospheric refractivity. Values of $\{H_i, N_{norm}\}$ can then be solved for, in a least square sense, to fit the $m_a + m_p$ measurements of bending and the complementary m_n values of N . Because the problem is severely non-linear, it is advantageous to eliminate the non-linearity by solving for the logarithm of the refractivity according to

$$\ln(N(r)) = \ln(N_{norm}) - \frac{r - R_j}{H_j} - \sum_{i=j+1}^{m_L} \frac{\Delta_i}{H_i} \quad (7)$$

as a function of $\{1/H_i, \ln(N_{norm})\}$. Similarly, the non linearity of Eq. (2) is damped by solving for the logarithm of the bending. However, since the reformulated problem is not completely linear, a few iterations are required before a solution is reached. At each iteration, k , we use the set $\{1/H_i^k, \ln(N_{norm}^k)\}$, Eq. (7) and a modified form of Eq. (2) to calculate the bending and refractivity. Evolution of the solution from one iteration to the next is accomplished by Taylor expanding around $\{1/H_i^k, \ln(N_{norm}^k)\}$. To first order, this can be expressed as

$$\begin{aligned} \ln(\alpha_m) &= \ln(\alpha_c(H_i, N_{norm})) + \sum \frac{\partial}{\partial p} \ln(\alpha_c(1/H_i, \ln(N_{norm}))) \Delta p \\ \ln(N_m) &= \ln(N_c(H_i, N_{norm})) + \sum \frac{\partial}{\partial p} \ln(N_c(1/H_i, \ln(N_{norm}))) \Delta p \end{aligned} \quad (8)$$

where $p = \{1/H_i, \ln(N_{norm})\}$

In the previous equations we used the subscript c to indicate computed quantities. The calculated α and N are then differenced from the observed bending and refractivity. Because of the non-linearity of the problem, it is beneficial to place some constraints on the allowed range of variation of Δp , so that the solution does not deviate very drastically from the linear regime. This is accomplished by introducing an *a priori* information matrix, taken to be diagonal and such that

$$\Lambda_i = \frac{1}{\text{cov}(p)} \quad (9)$$

$p = \{1/H_i, \ln(N_{norm})\}$

where $\text{cov}()$ indicates the parameters' covariance and it is chosen to be much larger than that of the measurements. It can be shown [Bierman, 1977] that the introduction of the information matrix can be interpreted as the addition of extra measurements, corresponding to the equation

$$\sqrt{\Lambda_i} \Delta p = 0 \quad (10)$$

Because the covariance $\text{cov}(p)$ is taken to be very large the extra measurements of Eq. (9) have no effect on the solution; nevertheless, introducing such measurements is crucial for the regularization of this problem, insuring that the system is always overdetermined. In particular, if no measurements are available, Eq. (10) yields the starting point as a solution.

The problem to be solved is cast into a matrix form which can be represented compactly as

$$\begin{pmatrix} \sqrt{\Lambda_i} \\ \text{partial}(\ln(\alpha)) \\ \text{partial}(\ln(N)) \end{pmatrix} \Delta p = \begin{pmatrix} 0 \\ (\ln(\alpha_m) - \ln(\alpha_c)) \\ (\ln(N_m) - \ln(N_c)) \end{pmatrix} \quad (11)$$

On the left-hand side of Eq. (11) the overall problem matrix is composed of a diagonal submatrix and two matrices; the first is upper triangular except for the rows corresponding to ‘positive elevation’ measurements, and both are obtained by calculating the partial derivatives of logarithm of bending and refractivity, respectively, with respect to $\{1/H_i, \ln(N_{\text{norm}})\}$. On the right-hand side of Eq. (11) are the discrepancies between measured and calculated α and N . The triangular-Householder with control algorithm [Bierman, 1977] is used to solve Eq. (11).

In the examples illustrated in this paper the starting values of $\{1/H_i^0, \ln(N_{\text{norm}}^0)\}$ are derived from an *a priori* model which is taken to be either the National Meteorological Center (NMC) stratospheric model or the European Center for Medium-range Weather Forecasts (ECMWF) global weather analyses available every six hours.

At each new iteration, the tangent point radius, r_{min} , associated with a given impact parameter a is obtained by recursively solving $a(r_{min}) = n(r_{min}) \times r_{min}$ using the latest solution. Knowledge of r_{min} is needed to recompute the bending measurements (Eq. 2) and the partials (Eq. 8). Even though the r_{min} 's can be changing as we iterate, the boundaries of the layers are fixed, and they are based on the initial layering scheme outlined above.

3. NUMERICAL RESULTS

3.1 Receiver Outside The Atmosphere

The first step in the validation of our technique consists of reproducing some refractivity profiles which have been previously derived with the Abel approach. We used data obtained from GPS/MET. We illustrate the comparisons in Figure 4 for one particular occultation.

For both inversion techniques, the fractional refractivity difference between GPS/MET and the ECMWF or NMC models are shown. Note that, except at very high altitudes, the Abel and raytracing techniques reproduce nearly the same retrievals with differences in absolute value $< (0.1-0.5\%)$. The larger differences occur near sharp changes in refractivity, where the raytracing routine appears to produce a somewhat smoother retrieval than the Abel inversion. At altitudes above 40 km, differences of about 1-5% are observed (Figure 4.b) between the Abel and JPL inversions.

Once refractivity is obtained, then temperature profiles in dry regions (upper troposphere and stratosphere) can be derived from the ideal gas law and hydrostatic equilibrium [Kursinski *et al.*, 1997]. In the lower and mid-troposphere, independent information of temperature can be used to derive accurate water vapor from refractivity [Kursinski and

Hajj, 1998]. In general, the refractivity information with associated covariance will be combined with independent information from an analysis (or something equivalent) with a corresponding covariance to make an optimal estimation of temperature and water vapor.

Temperature differences between the NMC model and the Abel and JPL inversions are shown in Figure 4.c, where water vapor in the lower troposphere is assumed to be that of the NMC. An initial value of temperature was needed in order to represent the mass above 50 km in the hydrostatic equilibrium integral and it was taken to be that of the NMC at 50 km, which explains the exact agreement of the retrievals and the model at that height. It was established elsewhere [see e.g. Kursinski et al., 1996; Ware et al., 1996] that temperature accuracy of GPS/MET are $<2\text{K}$ between 5-25 km. Larger T differences within these heights in Fig. 4 are reflective of errors in the NMC model. At altitude higher than 30 km (~ 10 mbar), Fig. 4 shows the JPL inversion to agree with NMC to better than 5K.

3.2 Receiver Inside The Atmosphere

3.2.1 Simulated Ascending Balloon

In order to validate the algorithm's ability to retrieve refractivity when the receiver is inside the atmosphere, we constructed a new set of measurements by starting with the occultation data used in the retrievals of Figure 4, and making the changes described as follows. First, we truncated the data set by excluding all measurements with tangent heights > 25 km. Second, we added 12 values of refractivity at heights above 25 km, weighed $1/5$ of the bending measurements. The values of N used here were obtained from the NMC model and extended in heights up to ~ 60 km. Third, we divided the observed bending angles by 2 to represent a receiver located at the tangent point for each link. The rationale behind the last step is that if the atmosphere is exactly spherically symmetric, then a receiver located at

the tangent point of the link would measure half the bending that it would measure from space. The situation we created is somewhat similar to carrying a GPS receiver on a balloon that collected GPS measurements up to 25 km altitude (but without positive elevation data). Figure 5.a shows the fractional refractivity difference between the NMC and the JPL inversion for the situation when the receiver is inside and outside the atmosphere (the latter is the same as the solid curve of Figure 4.b).

The almost perfect agreement between NMC and the “inside-the-atmosphere” retrieval above 30 km is not surprising since it is the NMC refractivity data which is driving the retrieval at these heights. However, the fact that the “inside-the-atmosphere” retrieval converges very rapidly to the “outside-the-atmosphere” retrieval indicates how focused the bending is near the tangent point. In fact, half of the bending occurs in the ~ 1.5 km region above the tangent point [Kursinski *et al.*, 1997], which implies that bending measurements are nearly localized at the layer where the tangent height is. Given that measurements constructed for the “inside-the-atmosphere” retrieval are equivalent to a receiver sitting at 25 km tracking the GPS at negative elevations, Figure 5.a indicates that there is a transition region of about 2-4 km below the receiver where the inversion is dependent on the *a priori* model. This is a large region if we are to apply this technique to a mountain top receiver. However, in the example of Figure 5, no data from positive elevations were included, which constrains the atmosphere above the receiver and could potentially eliminate or shorten that transition region. The inclusion of positive elevation data has been investigated and results are presented in the next sub-section. Temperature retrievals corresponding to Figure 5.a are shown in Figure 5.b.

3.2.2 Simulated Receiver on Mountaintop

The situation where a receiver is fixed at 5 km above the ground was simulated by constructing an artificial occultation event, introducing a set of arbitrary tangent heights ranging between 2-5 km. Taking the refractivity given by ECMWF to be the truth, a set of rays linking the transmitter to the receiver were constructed to pass through the specified tangent heights, and their bending angles were calculated. Similarly, a set of rays linking the transmitter to the receiver were constructed to correspond to positive elevation angles above the receiver horizon, and having impact parameter given by Eq. (1) where r is the radius of the receiver and ϕ is between 90° (0 deg. elevation) and 180° (zenith). Additional ‘measurements’ of refractivity above the receiver location were taken from the NMC model, again weighted much less than the bending measurements. Furthermore, the starting values for the parameter set were obtained from NMC also. Four different cases were considered, two at mid-latitudes and two in tropical regions, as illustrated in Table I. The “true” profiles of temperature and water vapor partial pressure (obtained from the ECMWF) used to generate the synthetic data set are shown in Figure 6.

An example of a synthetic data set of $\alpha(a)$ generated for case 4(see Table I) is shown in Figure 3.b. The top of Figure 3.b is magnified in order to illustrate some of the potentially complicated structure of this curve associated with atmospheric multipath ,which occurs when the signal travels along more than one path due to some sharp layers in the atmosphere. In particular, the $\alpha(a)$ structure of Figure 3.b shows that as the signal descends below 5 km, at some point it branches into three distinct signals coming from three different heights in the atmosphere as described in the occultation of Uranus’ atmosphere by *Lindal et al.* [1987]. This branching coincides with a very sharp layer of water vapor at about 3 km as illustrated in Figure 6 (case 4). The branching of the signal can be explained as follows. Before the signal reaches the top of the layer, there is only one ray in the atmosphere (ray 1). As ray 1 reaches the top of the layer, a second signal

appears simultaneously from the bottom of the layer and it branches into two signals, one moving upward (ray 2) and one moving downward (ray 3). Ray 1 and 2 merge together nearly at the peak of the layer, while ray 3 continues to go down into the atmosphere. Under certain conditions, the atmospheric inversion layer can block the signal for some time, giving a very clear indication of the height of the tradewind inversion [Hajj *et al.*, 1994].

In order to invert the synthetic data sets for the different cases, several numerical tests were performed to simulate possible strategies of complementing bending measurements with refractivity and understand their impact on retrievals. In the first test we assumed that the refractivity from NMC was specified directly above the receiver location and up to heights of about 60 km. Above 60 km the refractivity was extrapolated assuming an isothermal atmosphere. For this situation we quantified the effect of positive elevation bending measurements on the retrieval accuracy. The results are presented in Figures 7 and 8 for the cases of excluded and included positive elevation bending, respectively. When positive elevation bending measurements were included only angles up to 20° above the horizon were used because measurements at higher elevation were believed to have no strength in resolving the vertical structure.

In all cases we present the fractional error in the retrieved refractivity with respect to the “truth” (ECMWF) and, additionally, the fractional error of the first guess (NMC) with respect to the truth. Note that for the mid-latitude cases the first guess is relatively close to the truth, with discrepancies not exceeding 3% at heights below the receiver, whereas at tropical latitudes large deviations up to 15% are present. Figure 7 shows that the retrieval error is significantly less than the fractional difference between NMC and ECMWF below the receiver, and increases as the receiver height is approached, consistently with the requirement that at heights above the receiver the solution be given by NMC. The addition

of positive elevation bending measurements causes further reduction of the retrieval error, particularly around the receiver location, suggesting that they have sufficient strength to drive the inversion around the receiver location. It is noted that all bending measurements are weighted more than the refractivities by the retrieval algorithm.

To further understand the role of positive elevation bending measurements in retrieving refractivity profiles above the receiver location, we performed a second numerical test where we removed refractivity data for 20 km above the receiver, to simulate a more realistic case. An arbitrary number of layers was introduced in the region of the troposphere between 5 and 25 km, such that their thickness is about twice that of the layers below the receiver. The results are illustrated in Figure 9 for the four cases of Table I.

The figure shows a clear reduction of the retrieval error in a region above the receiver location extending at least a few km, beyond which the solution eventually matches the NMC, as expected. Although the test is limited the results are very encouraging and indicate that the positive elevation bending measurements can have enough strength to allow for a quite accurate retrieval of refractivity in the region above the receiver.

4. CONCLUSIONS

We have described and demonstrated a technique appropriate for inverting GPS occultation data to retrieve vertical profiles of refractivity, which could be used in assimilating the data into numerical weather models. Close agreement with the Abel results, in the applicable cases, confirms the correctness of the approach and implementation. Results presented for the simulated case of a receiver ascending through the atmosphere in a balloon and for a simulated receiver fixed at 5 km indicate that the accuracy of the retrieved refractivity below the receiver is good at and above the receiver location. Inclusion of positive elevation

bending data significantly improved the retrieved structure at most altitudes. In fact, inclusion of positive elevation bending data and simultaneous removal of *a priori* model refractivity below 25 km actually improved the accuracy of the results, clearly indicating that the model values were weighted too strongly relative to the data. More importantly, the results using positive elevation bending data means the retrieved vertical refractivity structure does not depend much on the accuracy of the model values to at least 5 km above the receiver altitude. This is a significant improvement over the results in Figure 5 which, as a result of not using positive elevation bending data, were significantly limited by the model accuracy down to an altitude at least 1 km below that of the receiver. The inclusion of positive elevation data, which enables us to retrieve refractivity up to a few kilometers above the receiver's height, implies that any mountain at the height of, or taller than, the boundary layer can be used as a vantage point to characterize the boundary layer structure. Accuracy and independence at and above the receiver location also mean that airplane results derived near the height of the airplane (defined as the altitude of interest) will be quite accurate and independent of *a priori* first guesses and may therefore significantly impact weather forecasting in the region. Although the conclusions drawn above are based on the examination of synthetically generated bending data, we feel encouraged by our very promising preliminary results and will pursue a validation with real data in the near future. Finally, it is important to note that even though we have validated this technique assuming a layered exponential model for the atmosphere, the approach can easily be generalized to include some horizontal variation of the gradient of refractivity.

ACKNOWLEDGMENTS

This work has been performed at the Jet Propulsion Laboratory, Pasadena, under contract with the National Aeronautical and Space Administration. This work was supported by NASA's Office of Earth Science.

REFERENCES

- Bierman G. J., *Factorization Methods for Discrete Sequential Estimation*, Academic Press, Inc., New York, 1997.
- Born, M., and E. Wolf, *Principles of Optics*, 122 pp., 6th ed., Pergamon, New York, 1980.
- Eyre J. R. Assimilation of radio occultation measurements into a numerical weather prediction system, European Center for Medium-Range Weather Forecasts, Tech. Memo. No. 199, May, 1994.
- Fjeldbo, G., A. J. Kliore, and V. R. Eshleman, The neutral atmosphere of Venus as studied with the Mariner V radio occultation experiments, *Astron. J.*, 76, 123-140, 1971.
- Gorbunov M.E., S. V. Sokolovsky and L. Bengtsson, Space refractive tomography of the atmosphere: modeling of direct and inverse problems, Max-Planck-Institut für Meteorologie, Hamburg, August 1996.
- Hajj, G. A., E. R. Kursinski, W. I. Bertiger, L. J. Romans, Assessment of GPS Occultations for Atmospheric Profiling, seventh conference on satellite meteorology and oceanography, pp. J7-J10, Monterey, CA, June 6-10, 1994.
- Hajj, G. A., E. R. Kursinski, W. I. Bertiger, S. S. Leroy, T. Meehan, L. J. Romans, and J. T. Schofield, Initial results of GPS-LEO occultation measurements of Earth's atmosphere obtained with the GPS/MET experiment, Proc. IAG Symp. G1, GPS Trends in Precise Terrestrial, Airborne, and Spaceborne Applications, IUGG XXI General Assy., Boulder, CO, 2-14 July 1995, Springer-Verlag, 1996.
- Kuo Y.-H., X. Zou, W. Huang, The impact of global positioning system data on the prediction of an extratropical cyclone-An observing system simulation experiment, *J. Dyn. Atmos. Ocean*, 27(1-4), 439-470, 1998.

- Kursinski, E. R., G. A. Hajj, K. R. Hardy, J. T. Schofield, and R. Linfield, Observing Earth's Atmosphere with Radio Occultation Measurements, *J. of Geophys. Res.*, Vol. 102, No. D19, pp 23429-23465, 1997.
- Kursinski, E. R., G. A. Hajj, K. R. Hardy, L. J. Romans and J. T. Schofield, Observing tropospheric water vapor by radio occultation using the Global Positioning System, *Geophys. Res. Lett.*, 22, 2365-2368, 1995.
- Kursinski, E. R., et al., Initial results of radio occultation observations of Earth's atmosphere using the Global Positioning System, *Science*, 271, 1107-1110, 1996.
- Kursinski E.R. and G. Hajj, An examination of water vapor derived from Global Positioning System occultation observations during June-July 1995, part I: Zonal means, submitted to *J. Geophys. Res.*, 1998
- Leroy S. S., Detecting Climate Signals: Some Bayesian Aspects, submitted to *J. Climate*, 1998.
- Leroy, S. S., Measurement of geopotential heights by GPS radio occultation, *J. Geophys. Res.*, 102, 6971-6986, 1997.
- Lindal, G. F., J. R. Lyons, D. N. Sweetnam, V. R. Eshleman, D. P. Hinson and G. L. Tyler, The atmosphere of Uranus: results of radio occultation measurements with Voyager 2, *J. Geophys. Res.*, 92, 14987-15001, 1987
- Rocken, C., R. Anthes, M. Exner, D. Hunt, S. Sokolovskiy, R. Ware, M. Gorbunov, W. Schreiner, D. Feng, B. Herman, Y.-H. Kuo, X. Zou, Analysis and validation of GPS/MET data in the neutral atmosphere, *J. Geophys. Res.*, 102(D25), 29,849-29,866, 1997.
- Tricomi F. G., *Integral Equations*, Dover Publications, Inc. New York, 1977.
- Ware, R., M. Exner, et al., GPS sounding of the atmosphere from low Earth orbit - preliminary results, *Bull. Am. Meteorol. Soc.*, 77, 19-40, 1996.

- Yuan, L. L., R. A. Anthes, R. H. Ware, C. Rocken, W. D. Bonner, M. G. Bevis and S. Businger, Sensing climate change using the global positioning system, *J. Geophys. Res.*, 98, 14,925-14,937, 1993.
- Zou X. F. Vandenberghe, B. Wang, M. E. Gorbunov, Y.-H. Kuo, S. Sokolovskiy, J. C. Chang, and J. G. Sela, Direct Assimilation of GPS/MET Refraction Angle Measurements: Part I: Concept and Results of Raytracing and Part II: Variational Assimilation Using Adjoint Techniques, submitted to *J. of Geophys. Res.*, 1998.

Figure Captions

Table I. Set of locations chosen to retrieve refractivity with receiver at 5 km

Figure 1: A pictorial view of GPS atmospheric sensing with a receiver inside the atmosphere

Figure 2: A pictorial view defining the variables for a GPS transmitter/receiver link

Figure 3: (a) Bending (left scale) and a (right scale) as a function of elevation for a receiver at 5 km altitude; (b) the same occultation of (a) showing the signal bending as a function of a (inverted scales); the inside plot is a magnification of the top portion of the plot; (c) bending vs. a for a space-based occultation

Figure 4: (a) Fractional refractivity difference between ECMWF model and GPS/MET data inverted with the Abel and JPL techniques (on the figure referred to as ALPHA); (b) same as in (a) but for the NMC model; (c) same as (b) but for temperature.

Figure 5: (a) Fractional refractivity difference between NMC and JPL inversion for a receiver inside and outside the atmosphere; (b) same as (a) but for temperature.

Figure 6. Temperature (left) and water vapor partial pressure (right) obtained from ECMWF at the four locations of Table I.

Figure 7. Fractional error in retrieved refractivity when positive elevation measurements are not included.

Figure 8. Fractional error in retrieved refractivity when positive elevation measurements are included.

Figure 9. Fractional error in retrieved refractivity when positive elevation measurements are included and no refractivity below 25 km is used.

Figure Captions

Table I. Set of locations chosen to retrieve refractivity with receiver at 5 km

Figure 1: A pictorial view of GPS atmospheric sensing with a receiver inside the atmosphere

Figure 2: A pictorial view defining the variables for a GPS transmitter/receiver link

Figure 3: (a) Bending (left scale) and a (right scale) as a function of elevation for a receiver at 5 km altitude; (b) the same occultation of (a) showing the signal bending as a function of a (inverted scales); the inside plot is a magnification of the top portion of the plot; (c) bending vs. a for a space-based occultation

Figure 4: (a) Fractional refractivity difference between ECMWF model and GPS/MET data inverted with the Abel and JPL techniques (on the figure referred to as ALPHA); (b) same as in (a) but for the NMC model; (c) same as (b) but for temperature.

Figure 5: (a) Fractional refractivity difference between NMC and JPL inversion for a receiver inside and outside the atmosphere; (b) same as (a) but for temperature.

Figure 6. Temperature (left) and water vapor partial pressure (right) obtained from ECMWF at the four locations of Table I.

Figure 7. Fractional error in retrieved refractivity when positive elevation measurements are not included.

Figure 8. Fractional error in retrieved refractivity when positive elevation measurements are included.

Figure 9. Fractional error in retrieved refractivity when positive elevation measurements are included and no refractivity below 25 km is used.

case#	latitude(°)	longitude(°)
1	40	180
2	34	-120
3	20	-160
4	-10	40

Table I. Set of locations chosen to retrieve refractivity with receiver at 5 km

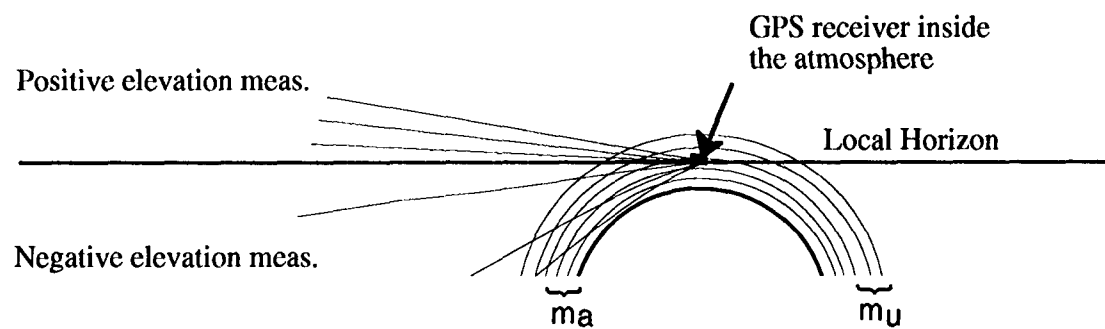


Figure 1: A pictorial view of GPS atmospheric sensing with a receiver inside the atmosphere

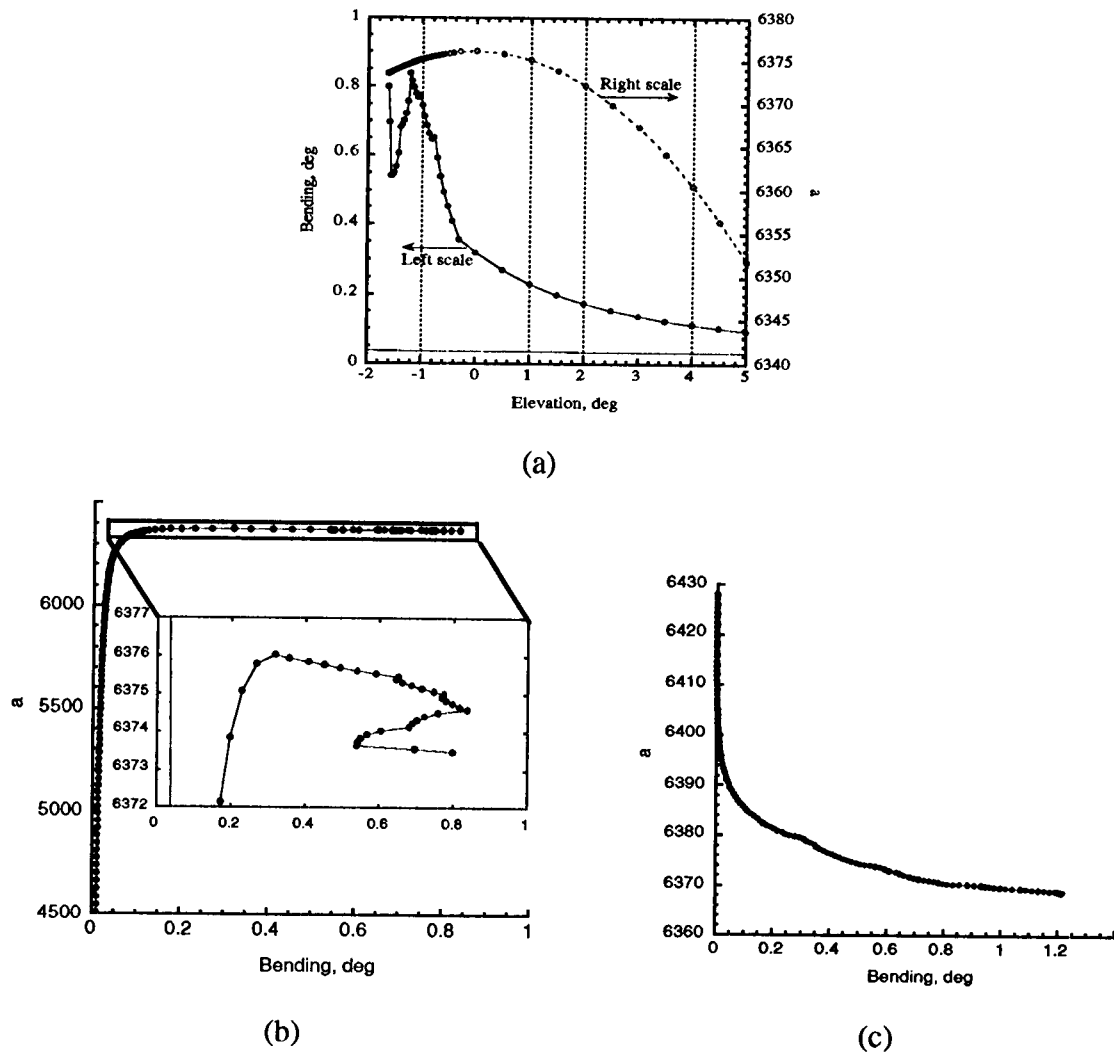
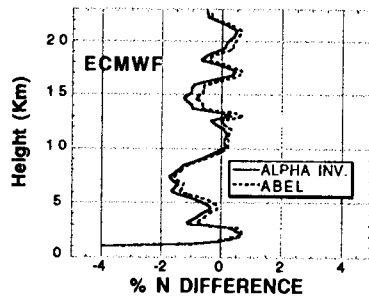
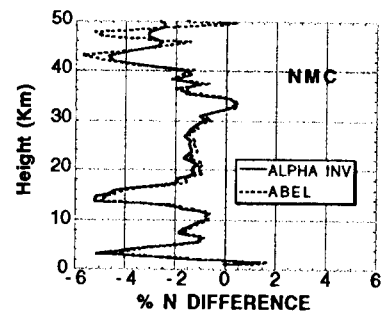


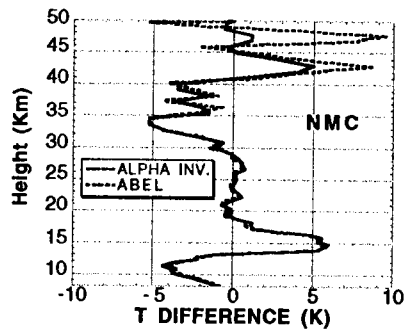
Figure 3: (a) Bending (left scale) and a (right scale) as a function of elevation for a receiver at 5 km altitude; (b) the same occultation of (a) showing the signal bending as a function of a (inverted scales); the inside plot is a magnification of the top portion of the plot; (c) bending vs. a for a space-based occultation



(a)

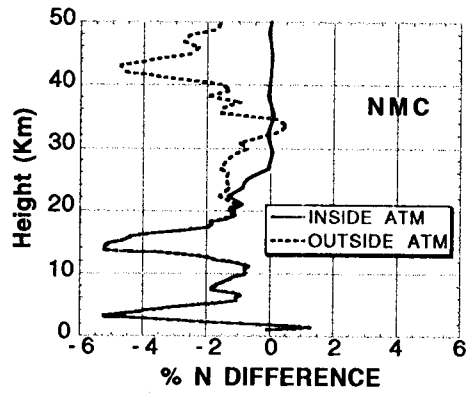


(b)

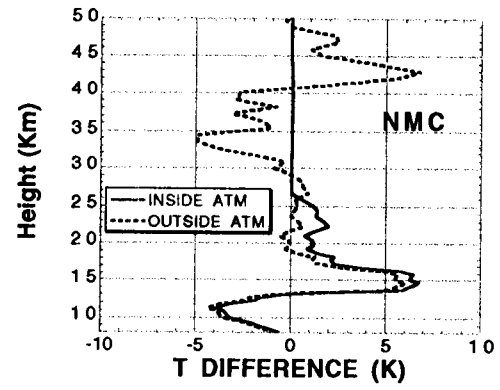


(c)

Figure 4: (a) Fractional refractivity difference between ECMWF model and GPS/MET data inverted with the Abel and JPL techniques (on the figure referred to as ALPHA); (b) same as in (a) but for the NMC model; (c) same as (b) but for temperature.



(a)



(b)

Figure 5: (a) Fractional refractivity difference between NMC and JPL inversion for a receiver inside and outside the atmosphere; (b) same as (a) but for temperature.

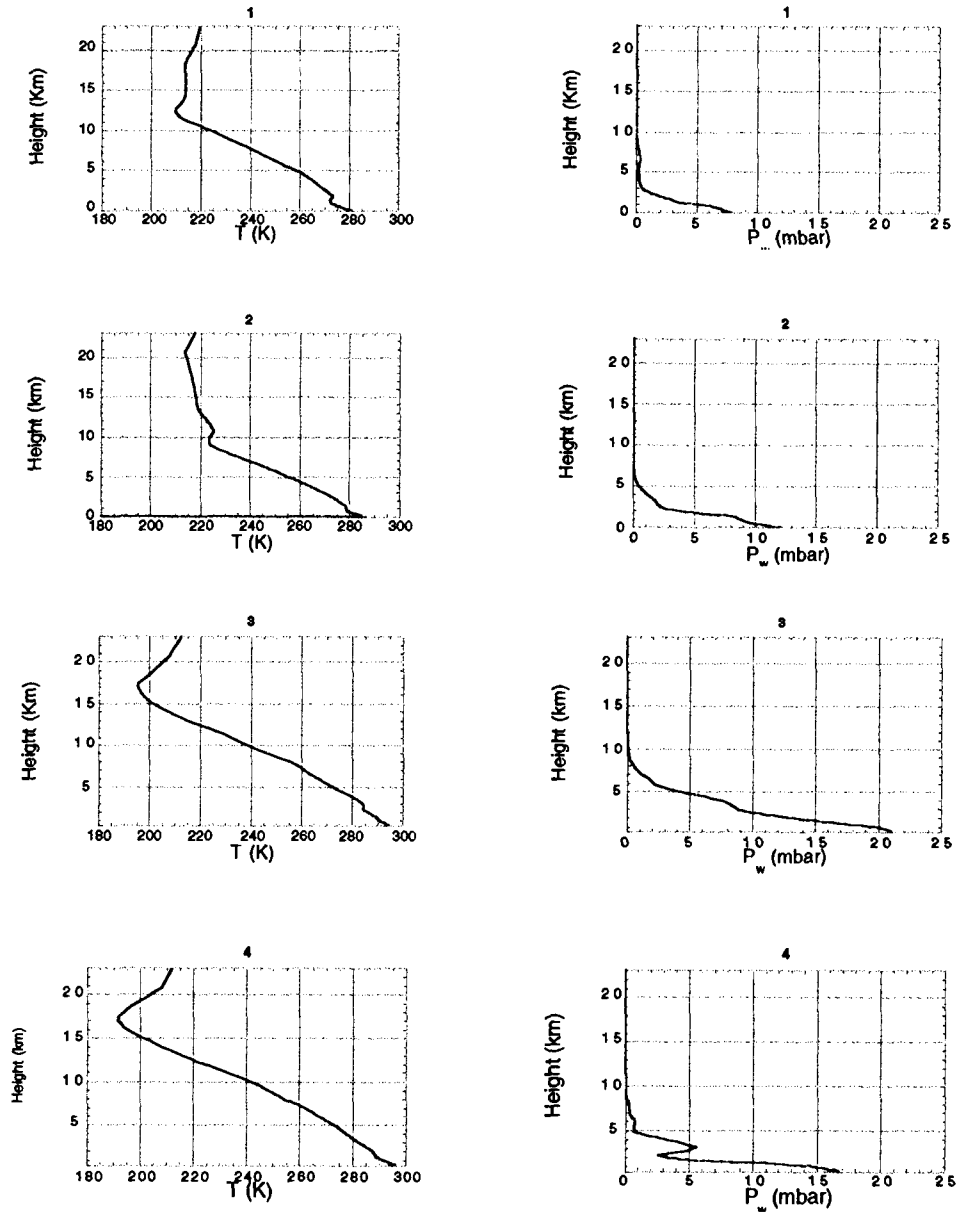


Figure 6. Temperature (left) and water vapor partial pressure (right) obtained from ECMWF at the four locations of Table I.

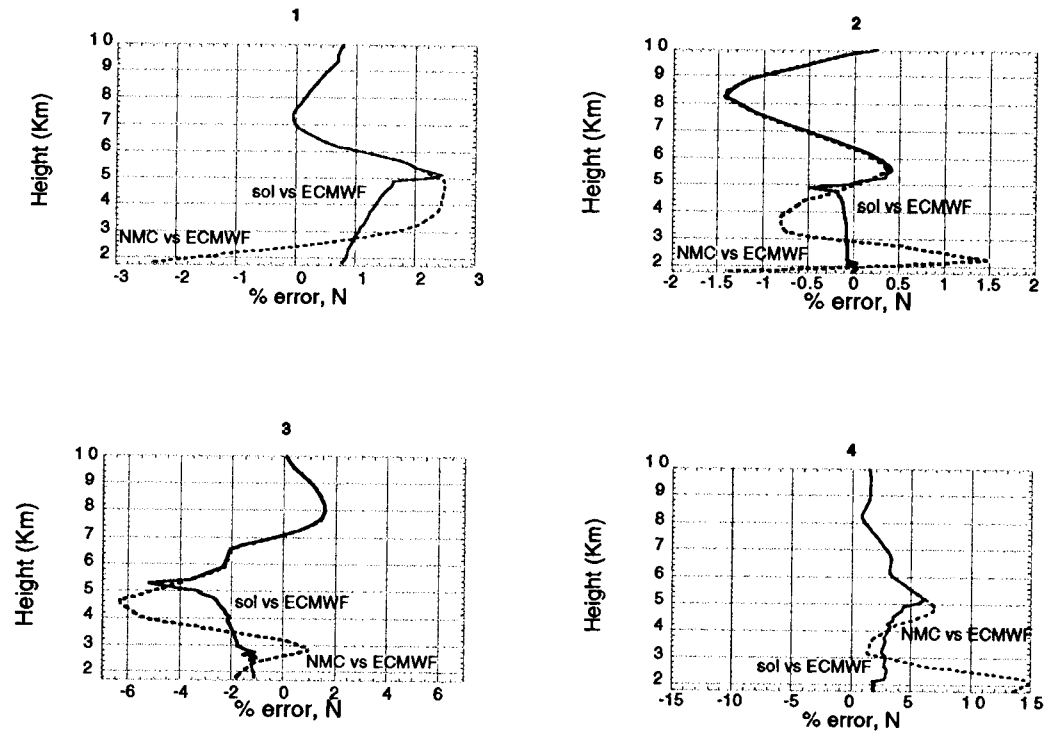


Figure 7. Fractional error in retrieved refractivity when positive elevation measurements are not included.

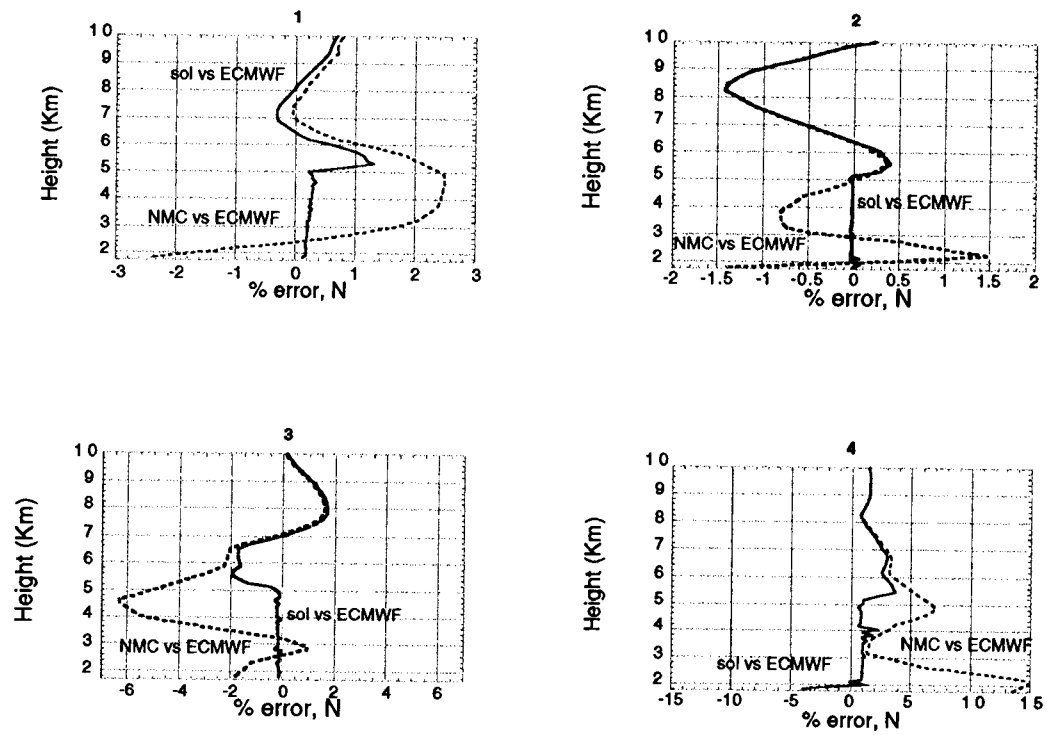


Figure 8. Fractional error in retrieved refractivity when positive elevation measurements are included.

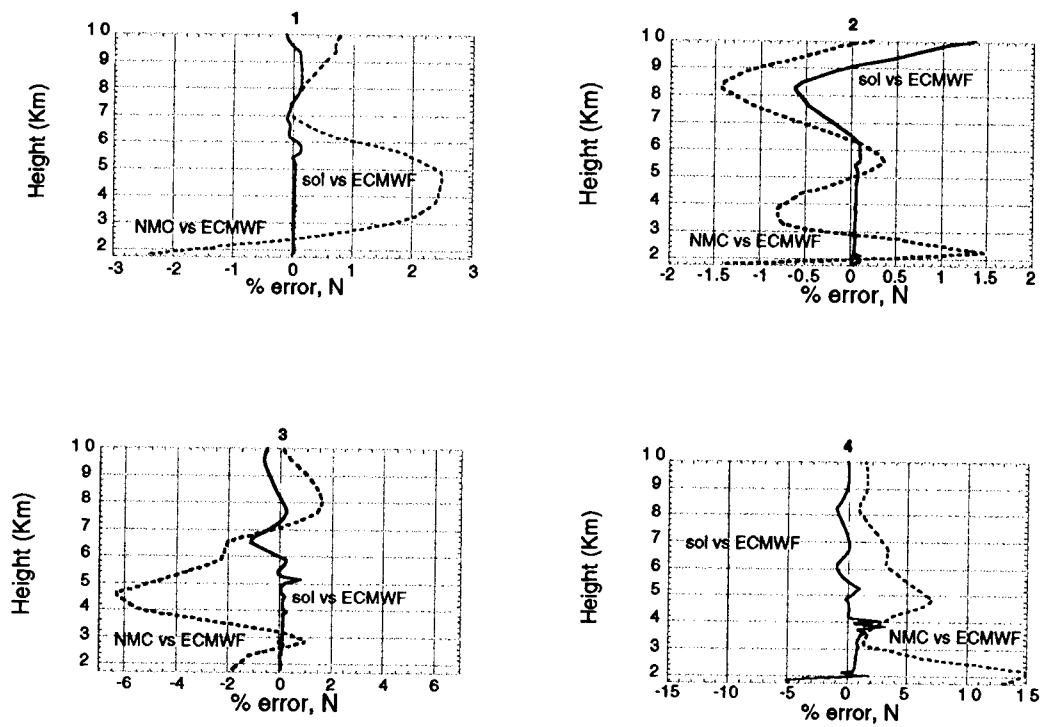


Figure 9. Fractional error in retrieved refractivity when positive elevation measurements are included and no refractivity below 25 km is used.